JGR Atmospheres

RESEARCH ARTICLE
10.1029/2022JD037751

Key Points:

- Mesospheric gravity-wave activity at two Antarctic stations was larger in winter than in spring and fall
- Wave activity at Davis was not significantly different with Syowa in winter but smaller in fall, which can be explained by filtering effect
- We find that GWs at Davis on 29 August 2016, were very likely generated by a spontaneous adjustment and/or a tropospheric jet wave breaking

Correspondence to:
M. Kogure,
kogure.masaru.055@m.kyushu-u.ac.jp

Citation:
Kogure, M., Nakamura, T., Murphy, D. J., Taylor, M. J., Zhao, Y., Pautet, P.-D., et al. (2023). Characteristics of gravity wave horizontal phase velocity spectra in the mesosphere over the Antarctic stations, Syowa and Davis. *Journal of Geophysical Research: Atmospheres*, *128*, e2022JD037751. https://doi.org/10.1029/2022JD037751

Received 28 AUG 2022
Accepted 25 FEB 2023

Characteristics of Gravity Wave Horizontal Phase Velocity Spectra in the Mesosphere Over the Antarctic Stations, Syowa and Davis

Masaru Kogure[1], Takuji Nakamura[2,3], Damian J. Murphy[4], Michael J. Taylor[5], Yucheng Zhao[5], Pierre-Dominique Pautet[5], Masaki Tsutsumi[2,3], Yoshihiro Tomikawa[2,3,6], Mitsumu K. Ejiri[2,3], and Takanori Nishiyama[2,3]

[1]Department of Earth and Planetary Science, Kyushu University, Fukuoka, Japan, [2]National Institute of Polar Research, Tachikawa, Japan, [3]Department of Polar Science, SOKENDAI (The Graduate University for Advanced Studies), Tachikawa, Japan, [4]Australian Antarctic Division, Department of Agriculture, Water and the Environment, Kingston, TAS, Australia, [5]Center for Atmospheric and Space Sciences, Physics Department, Utah State University, Logan, UT, USA, [6]Polar Environment Data Science Center, Research Organization of Information and Systems, Tachikawa, Japan

Abstract Mesospheric gravity-wave (GW) phase velocity spectra and total powers at two Antarctic stations, Davis and Syowa, were derived using OH airglow data from March to October in 2016. The total powers have similar seasonal variation, that is, maxima in winter at both stations. The average powers at both stations in winter were not significantly different. However, the power at Davis in September was three times smaller than that at Syowa. This lower power at Davis was attributed to GWs with omnidirectional phase velocity. These lower GW activities at Davis could be attributed to a longitudinal variation in wave filtering; a stronger wind at Davis filtered out more GWs than at Syowa. Also, to explore possible sources in the middle atmosphere, we investigated one event, in which GWs with ∼100 ms^{-1} southeastward phase velocity appeared at Davis on 29 August. The raytracing method was applied, and its result indicated that those GWs with high southeastward phase velocity propagated from ∼45 km altitude or higher over the Southern Ocean. A large residual of the non-linear balanced equation was found at 50 km on its ray path. GWs, very likely emitted from a tropospheric jet, were also found near the ray path at the termination altitude over the Southern Ocean and possibly appeared saturated between 45 and 50 km. Therefore, the OH imager at Davis probably captured GWs generated by a spontaneous adjustment in the upper stratosphere and/or secondary GWs produced by the breaking of the GWs that have originated from the tropospheric jet.

Plain Language Summary A gravity wave (GW) is a type of atmospheric wave that transports momentum from the Earth's surface to the edge of the atmosphere where it can drive atmospheric circulations. The temporal and spatial variation of GWs is not well understood, and their sources remain unclear. We observed GWs at the upper edge of the atmosphere over two Antarctic stations (Syowa and Davis) and calculated their phase velocity and total power spectra. The total powers have winter maxima at both stations. Although the average powers at both stations in winter were not significantly different, the power at Davis in September was three times smaller than that at Syowa. The lower GW activity at Davis could be attributed to a stronger wind at Davis, which filtered out more GWs than at Syowa. Also, to explore possible sources in the middle atmosphere, we investigated one event at Davis on 29 August 2016. We found that some GWs propagated from ∼45 km altitude or higher over the Southern Ocean. Those GWs could be emitted from the polar night jet (flow imbalance) and/or secondary GWs produced by the breaking of the GWs that have originated from the tropospheric jet.

1. Introduction

Gravity waves (GW) play an essential role in transporting momentum vertically and driving the circulation in the middle atmosphere (Fritts & Alexander, 2003). Current global circulation models (GCMs) cannot resolve the full spectrum of GWs so that GW influences (GW drags) are parametrized in GCMs. Although the GW drag parameterization schemes improve the ability of GCMs to reproduce observations, they still poorly represent GW sources, spectra, local variability, and intermittency, which causes deviations between GCMs and the real atmosphere (Alexander et al., 2010). Inadequate knowledge of GWs is a key element of this limitation.

Table 1
Summary of the Two Airglow Imager Specifications

Station	Latitude	Longitude	Operation institution	Airglow[a]	Sampling interval[b]	Exposure	Detector size[c]
Syowa	69°S	40°E	NIPR	OH (0.9–1.7 μm)	5 s	2 s	320 × 256
Davis	69°S	78°E	USU	OH (0.9–1.7 μm)	10 s	3 s	320 × 256

[a]The OH layer altitude is assumed as 87 km. [b]OH intensity images are averaged in 1 min. [c]256 × 256 pixels in the center of an image are used for this analysis.

In order to understand GW sources and features, many studies have investigated GWs in the real atmosphere by using in situ and remote sensing instruments. Airglow imaging is one remote sensing method that has high sensitivity to GWs with small horizontal wavelengths (~10s km) and short ground-based periods (several minutes). Such GWs deposit substantial momentum around the mesopause (Fritts & Vincent, 1987).

Matsuda et al. (2017) investigated the spatial variability of GW horizontal phase velocity around the edge of Antarctica by using observations from four OH airglow imagers during 1.5 months (April–May) at Syowa (69° S, 40° E), Davis (69° S, 78° E), McMurdo (78° S, 167° E), and Halley (76° S, 26° E). These instruments which are operated by the Antarctic Gravity Wave Instrument Network showed that GW intermittency can be caused by the wind filtering effect, and the GW activity over the Antarctic was variable in latitude (the GW activity at Syowa and Davis were ~five times larger than those at McMurdo and Halley). They also found that the GW power spectral density (PSD) for waves with eastward phase velocities less than ~ 70 ms^{-1} was ~10 times larger at Davis than at Syowa. This large PSD at Davis was exceptional because the GWs with small eastward phase velocity could not reach the airglow layer from the troposphere at Davis, as well as Syowa. The paper mentioned that a possible source of those GWs may be secondary generation above the stratosphere, although it does not robustly demonstrate the possible source. Also, it is uncertain whether the large PSD in the eastward velocity is a common feature at Davis because of the short (1.5 month) data set.

The purpose of this study is to investigate common/different features in phase velocity spectra between Davis and Syowa in more detail than Matsuda et al. (2017) and to show seasonal variation at both locations during a whole austral winter season (March–October) in 2016. Also, this study is to explore possible sources in the Antarctic middle atmosphere. Chapter 2 introduces OH airglow imagers at Syowa and Davis, and data analysis. In Chapter 3, we show the common/different features in GW activity between Syowa and Davis and compare our results with Matsuda et al. (2017). In Chapter 4, we discuss the effects of filtering (including critical and turning level filtering) on the GWs and investigate a source of GWs with eastward phase velocity in the Antarctic middle atmosphere.

2. Observation and Data Analysis

Two OH airglow imagers at Syowa (40°E, 69°S) and Davis (78°E, 69°S) are operated by National Institute of Polar Research and the Utah State University, respectively. Both imagers are equipped with indium gallium arsenide (InGaAs) detectors, which are sensitive to wavelengths between 0.9 and 1.7 μm, avoiding a large part of the auroral contamination (0.4–0.8 μm) seen by CCD detectors (Matsuda et al., 2017). The detectors are incorporated with a Fujinon FE185C086HA-1 C-mount fisheye lens to observe the whole sky. The specification of both imagers is summarized in Table 1. This study used the data without clouds, moon, and auroral contamination lasting for more than 1 hr from March to October 2016. Table 2 shows the distribution of the data windows, and this study analyzed 39 days at Syowa and 55 days at Davis.

To derive a GW PSD in the phase velocity domain, an M-transform was applied to the OH airglow movie each night. Since the M-transform is described in Matsuda et al. (2014, 2017) and Perwitasari et al. (2018) in detail, only preprocesses are explained here. The raw image data were averaged to 1 min for compatibility between measurement cadences at Syowa and Davis and star and dark count removal was applied. To derive relative OH airglow intensity perturbations, the average nighttime intensity is subtracted from each 1 min image, the residual intensity (I') was divided by the nightly mean (I_0), and then I'/I_0 was defined as the relative intensity

Table 2
The Number of Data Windows Used in This Study

		March	April	May	June	July	August	September	October	Total
Syowa	Number of night	1	8	9	3	4	7	6	1	39
	Total length (hour)	1	17.9	35.7	11.4	14.8	23.5	12.2	1.3	117.5
Davis	Number of night	6	6	7	2	8	11	10	5	55
	Total length (hour)	15.4	12.3	15.8	12.8	26	56	27.6	10.6	176.5

Note. The criteria for choosing the data are (a) clear-sky, (b) without the moon, and (c) aurora-free images continued for >1 hr.

perturbation. The I'/I_0 images were projected onto geographical coordinates, assuming a mean emission height of 87 km altitude (Baker & Stair, 1988). An OH emission height can vary between 79 and 88 km altitudes (Grygalashvyly et al., 2014; Nishiyama et al., 2021), but this causes less than 10% phase speed error, and the error can be neglected in this study. The M-transform was applied to each $256 \times 256\,\mathrm{km}^2$ area for each night movie, centered on the zenith, with $1 \times 1\,\mathrm{km}^2$ pixel size. The spectral components with 5–100 km horizontal wavelengths, 8–60 min ground-based periods, and 0–150 ms^{-1} phase speeds were extracted and regarded as representing GW intensities.

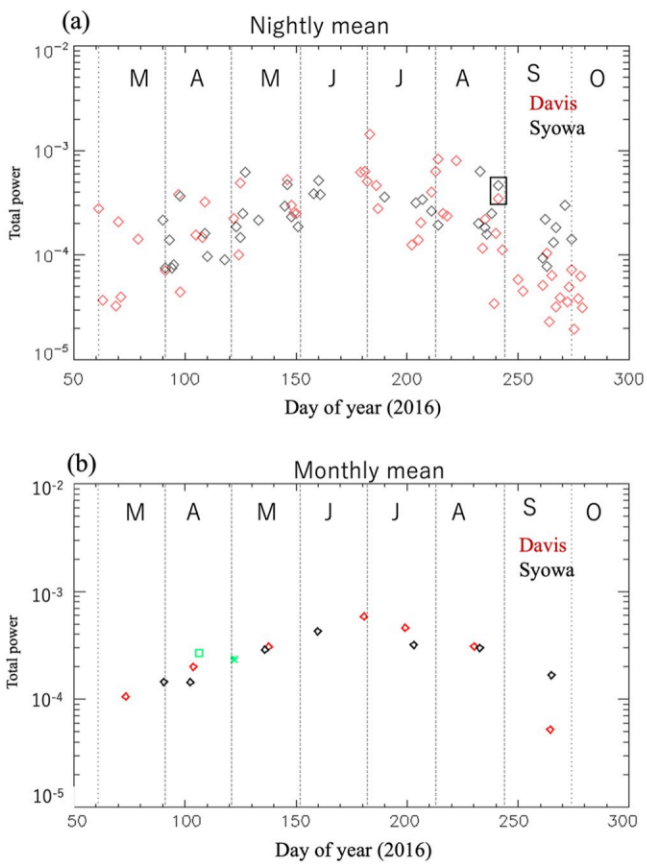

Figure 1. (a) The red and black diamonds indicate nightly mean total average powers of gravity-waves at Davis and Syowa, respectively. The black box indicates an event on 29th August which is discussed in chapter 5. (b) The red and black diamonds are same as (a) but monthly mean. The green square and asterisk indicate the total power averaged in April–May 2013 at Davis and Syowa, respectively, quoted from Matsuda et al. (2017). The *x* axis indicates a center of observation day weighted with the total power.

3. Comparison of GW Activities Between Syowa and Davis

Figure 1 shows total powers of the GWs, obtained using the PSD integrated in direction and phase speed from 0 to 150 ms^{-1}, over Davis and Syowa stations. The GW activity over both stations increased from March–April (fall) to May–August (winter) by 2–3 times and decreased in September–October (spring). The total powers have similar and comparable seasonal variations in Figure 1a. It should be noted that the powers in June and July are larger at Davis than at Syowa by $\sim 1 \times 10^{-4}$, but this difference is probably attributed to a data gap from the middle of June to early July in Syowa. On the other hand, the total power in September over Davis was almost three times smaller than that over Syowa. Since the centers of observation days in September are almost the same (~270) at both stations, the difference in September seems to be attributed to a dynamical mechanism and will be discussed later. The monthly mean values in April and May at Syowa and Davis in 2016 are $1.5 - 2.5 \times 10^{-5}$ and comparable with ones averaged in April–May 2013 at the two stations reported by Matsuda et al. (2017). Therefore, the total average powers at Syowa and Davis were not significantly different in fall to winter, but the one at Davis was three times smaller than that at Syowa at least in 2016.

To further explore the characteristics of the GWs at Davis and Syowa, the average phase velocity spectra for May–August (winter) and September are shown in Figure 2. The spectra for Syowa and Davis in Figures 2a–2d have the same directionality; that is, for phase speeds $\lesssim 50\,\mathrm{ms}^{-1}$, the PSD between $180 - 360°$ clockwise from the north (westward) is larger than that in the same speed range between $0 - 180°$ clockwise (eastward). For phase speeds $\geq 80\,\mathrm{ms}^{-1}$, the result is reversed; that is, the PSD magnitude is larger in the eastward phase speed domain than in the westward domain. Those directionalities can be explained by a filtering effect around the polar night jet region; the strong eastward wind filters out GWs with $\lesssim 50\,\mathrm{ms}^{-1}$ eastward phase velocity by critical level and $\geq 80\,\mathrm{ms}^{-1}$ westward phase velocity by turning

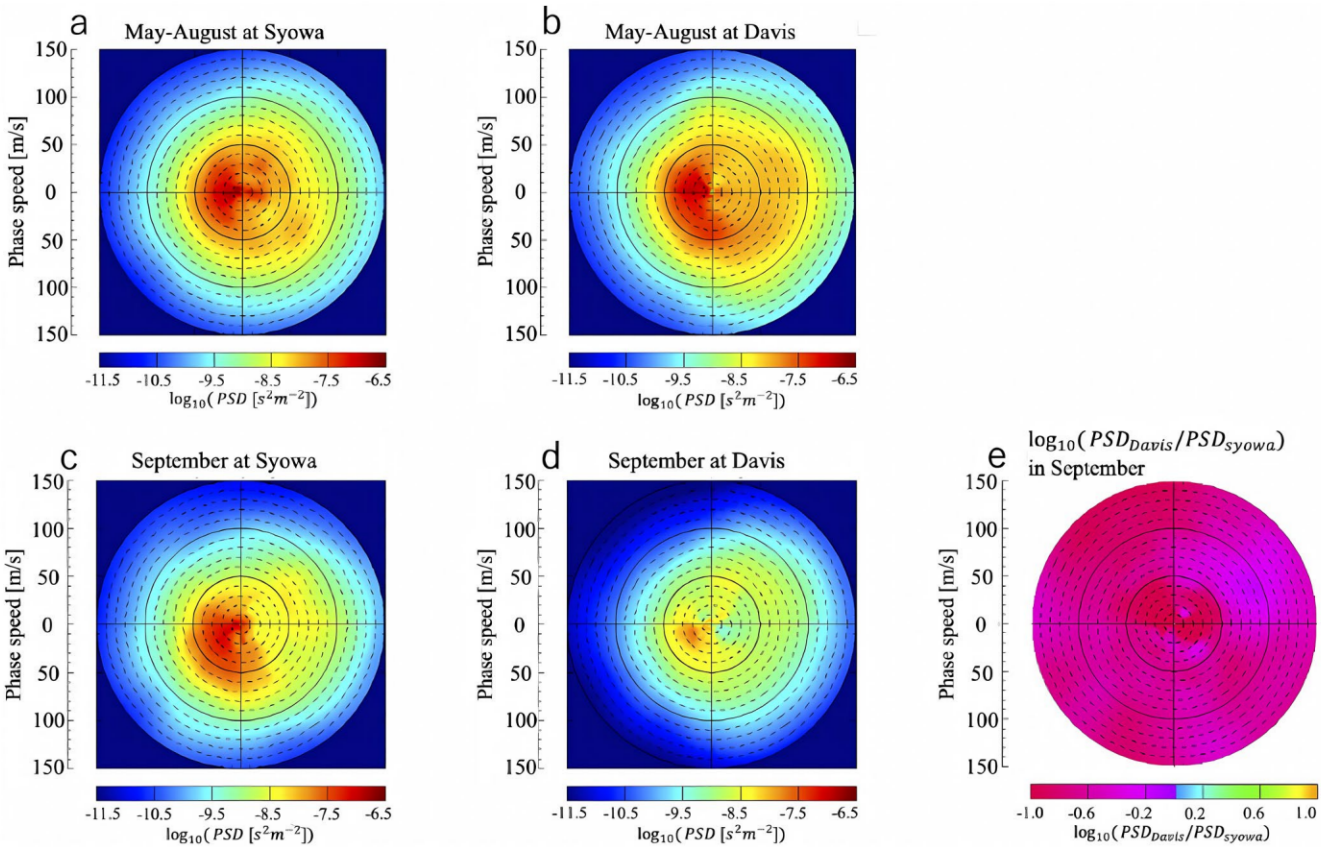

Figure 2. Power spectral density (PSDs) averaged in May–August and September at Syowa (a) and (b) and Davis (c) and (d), respectively. Phase speed lines are separated by 10 ms^{-1}. The panel (e) shows the ratio between the PSDs at Syowa and Davis in September.

level (cf. Tomikawa, 2015). However, magnitudes of the PSD in September are lower at Davis than at Syowa; indeed, the spectral ratio (PSD_{Davis}/PSD_{Syowa}) in Figure 2e shows that the PSD at Davis is smaller in the whole phase velocity domain than that at Syowa, implying the lower total power at Davis was attributed to the lower PSD in the whole domain during September. These differences can be caused by the filtering effect, so that the difference of filtering effect between both stations will be discussed in the next chapter.

4. Comparison Between GW Spectra and Probability Diagrams of Wave Transmission

To evaluate the filtering effect, we compare the GW phase velocity spectra with "probability diagrams" of wave transmission. These probability diagrams were calculated as follows. First of all, transmission during the observation time is calculated from a wind and buoyancy frequency at each hour in accordance with Tomikawa (2015). This transmission implies the possibility of vertical propagation, for a GW on a phase velocity spectrum, from an altitude of a wave emission up to the airglow layer altitude. The wave source and airglow altitudes are assumed to be 10 and 87 km, respectively. The winds and buoyancy frequencies below 70 km altitude are from The Modern-Era Retrospective Analysis for Research and Applications, Version 2, that is, MERRA-2, (Gelaro et al., 2017). The values between 70 km and the top of MERRA-2 are averages calculated, with a linear weighting function between MERRA-2 and observations, MF radars (Tsutsumi et al., 2001) and Aura Microwave Limb Sounder (MLS) (Waters et al., 2006). Those above the top of MERRA-2 were from the observations. Figure 3 shows the winds and buoyancy frequencies averaged in May–August and September at each station and their standard deviations. Finally, total transmission time is divided by the total observation time. Since the probability diagram can represent a temporal variation of the filtering effect, this diagram represents more realistic filtering in the long term than the transmission diagram calculated from a background condition averaged over a long duration. Tomikawa (2015) pointed out that the propagation possibility significantly depends on a GW ground-based period so that the spectra in Figure 2 were divided into six ground-based period bands in accordance with Matsuda et al. (2017).

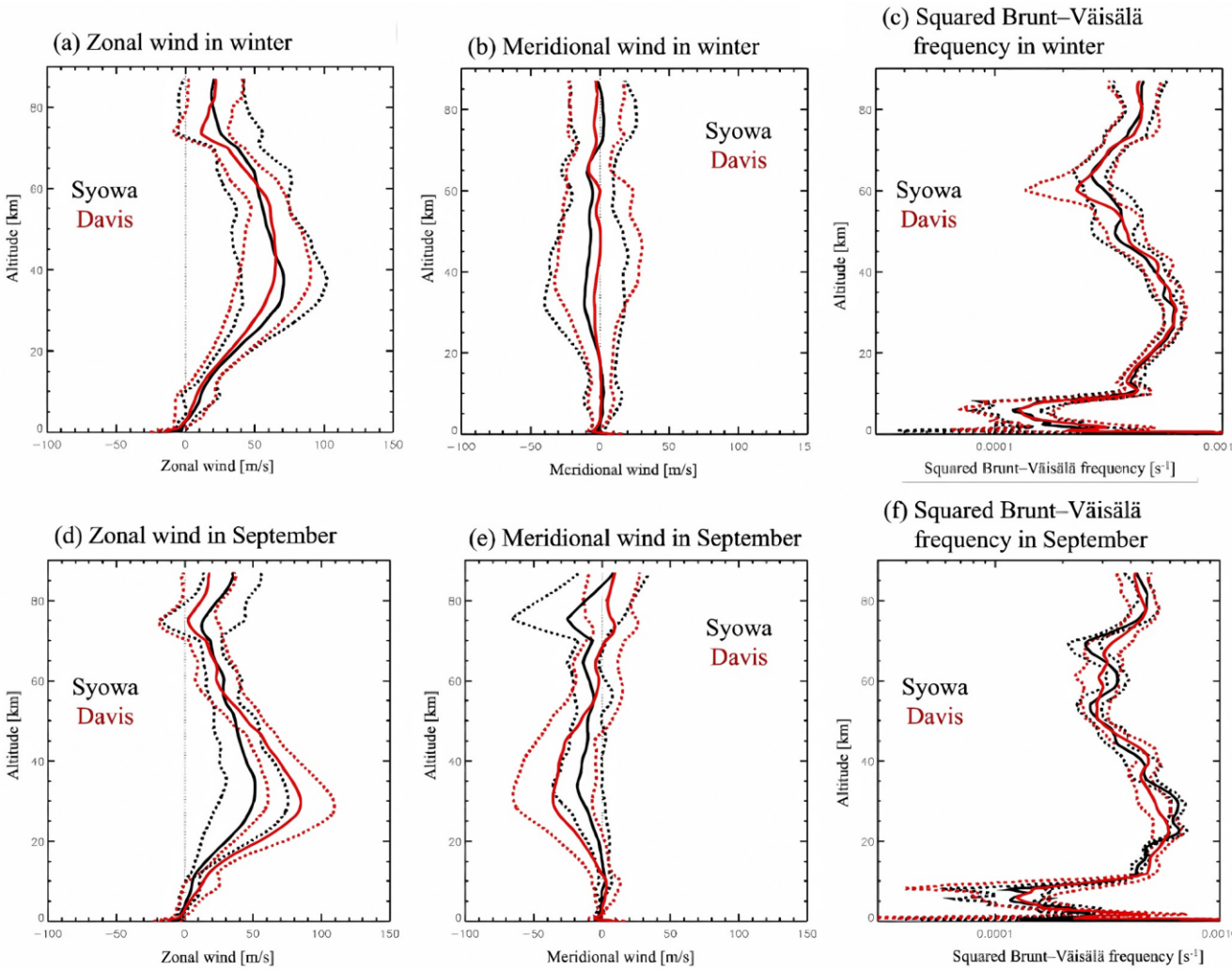

Figure 3. (a) Zonal and (b) meridional wind, and (c) squared buoyancy frequency profiles averaged in observation time during winter (from May to August) in Syowa (black) and Davis (red), respectively. The solid lines indicate their mean values, and the dashed lines indicate their standard deviation. (d), (e), and (f) are the same as (a), (b), and (c), respectively, but in September.

Figure 4 shows the comparison between the average spectra and probability diagrams of wave transmission in May–August (winter). The background filtering effects over each ground-based period range are almost the same at both stations; that is, the winter middle atmosphere always filtered GWs with westward phase velocity with very short ground-based periods (8–16 min) and GWs with eastward phase velocity less than ~70 ms^{-1} in the over all ground-based periods. This result supports the inference that the aforementioned feature of the spectra in Syowa and Davis (large PSDs in the high eastward and low westward phase velocity domains) is attributed to the filtering effect due to the strong eastward wind of the polar-night jet. Indeed, the winter mean eastward winds are more than 60 ms^{-1} around 40 km at both stations (Figure 3a). It should be noted that PSDs with westward phase velocity less than ~50 ms^{-1} and with 8–16 min ground-based periods were enhanced at both stations despite being in a low propagation probability region. This result suggests that those GWs were generated above 10 km altitude (i.e., stratosphere and/or mesosphere). One of the possible sources in the middle atmosphere is the saturation of large-scale (long ground-based period) GWs in situ in the OH layer (Bossert et al., 2017; Franke & Robinson, 1990; Heale et al., 2017; Snively & Pasko, 2003). The enhanced PSDs with long ground-based period bands (41–60 min) with ≤~50 ms^{-1} westward phase velocity suggests the saturation of the GWs with the long ground-based period bands and generation of small-scale secondary GWs. Because the PSDs in the 6 ground-based period bands were enhanced in the same westward phase velocity domain (≤~50 ms^{-1}), we speculate that the enhanced PSDs in short ground-based period bands were attributed to higher harmonic Fourier components of the GWs with the long ground-based period bands.

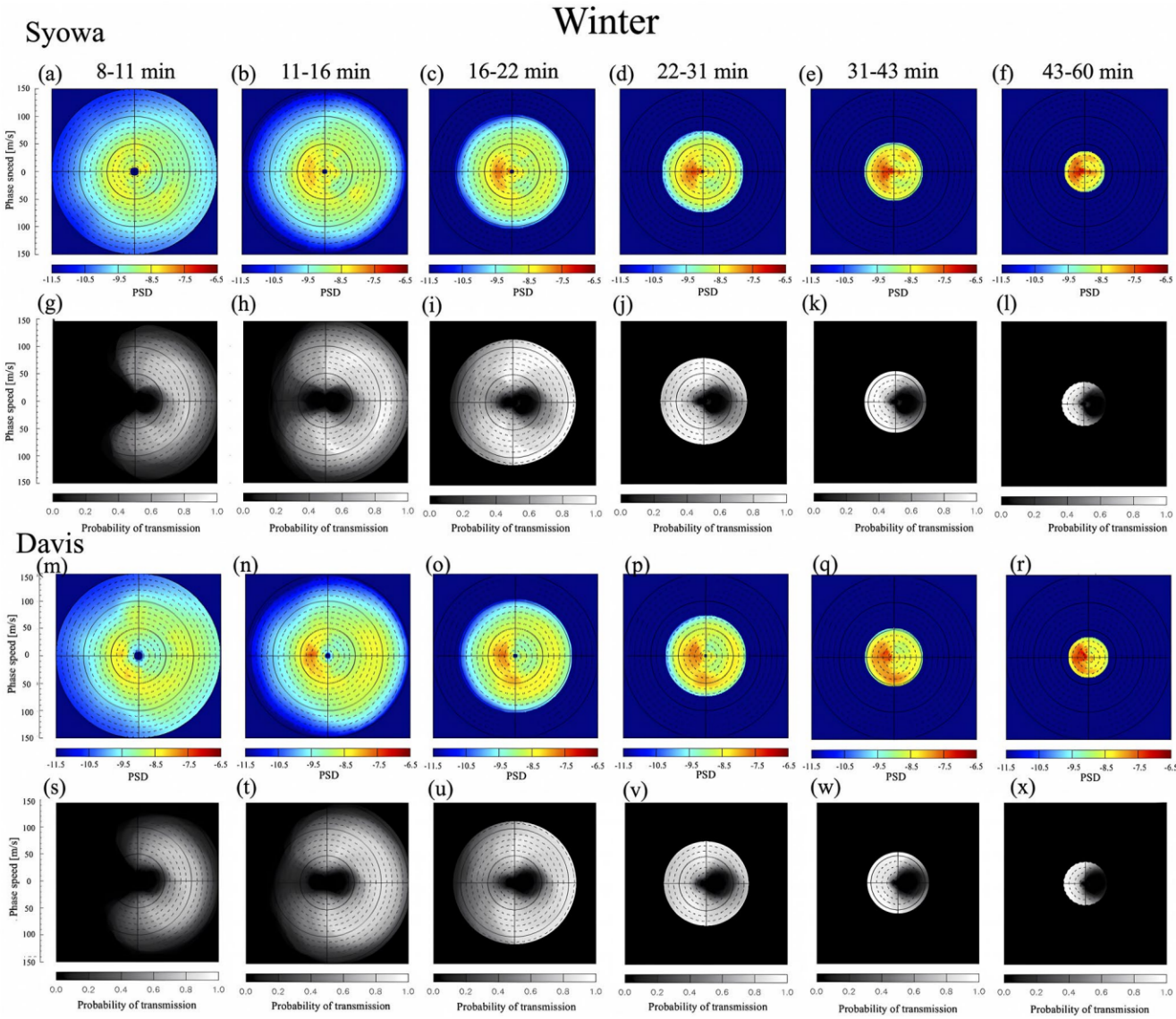

Figure 4. Comparison between the average spectra and probability diagrams in May–August (winter). The color plots in the first (a-f) and third (g-l) rows indicate the mean spectra in Syowa and Davis, respectively, in ground-based period ranges of 8–11, 11–16, 16–22, 22–31, 31–43, and 43–60 min. The black-and-white plots in the second (m-r) and fourth (s-x) rows are the same as the ones in the first and third rows except for the probability diagrams.

Other possible mechanisms are primary GW breaking, or instability in the polar night jet in the middle atmosphere. Transmission from a distant (unfiltered) wave source via a wave duct is one of the possible mechanisms, as well.

On the other hand, the propagation probabilities in September are higher in Syowa than in Davis (Figures 5g–5l and 5s–5x, and 5x). For example, the propagation probability of GWs with 11–16 min ground-based period and 50–80 ms^{-1} southeastward phase velocity is more than 70% at Syowa but less than 40% at Davis. It is consistent with the spectra in which the PSDs in that direction at Syowa ($PSD \sim -8.5$) are larger than Davis ($PSD \sim -9.5$). Those results suggest that the weaker total power in September over Davis is attributed to the filtering effect. This intense filtering effect at Davis is attributed to the stronger wind in the stratosphere, because Figures 3d and 3e show the mean zonal and meridional winds are larger in Davis than Syowa by ~20 and ~30 ms^{-1}, respectively, around 30 km altitude.

5. Event Study for GW Originated From the Middle Atmosphere

Some studies (Kam et al., 2021; Matsuda et al., 2017; Rourke et al., 2017) have shown that OH imagers sometimes capture GWs originating from the Antarctic middle atmosphere although their sources remain unclear.

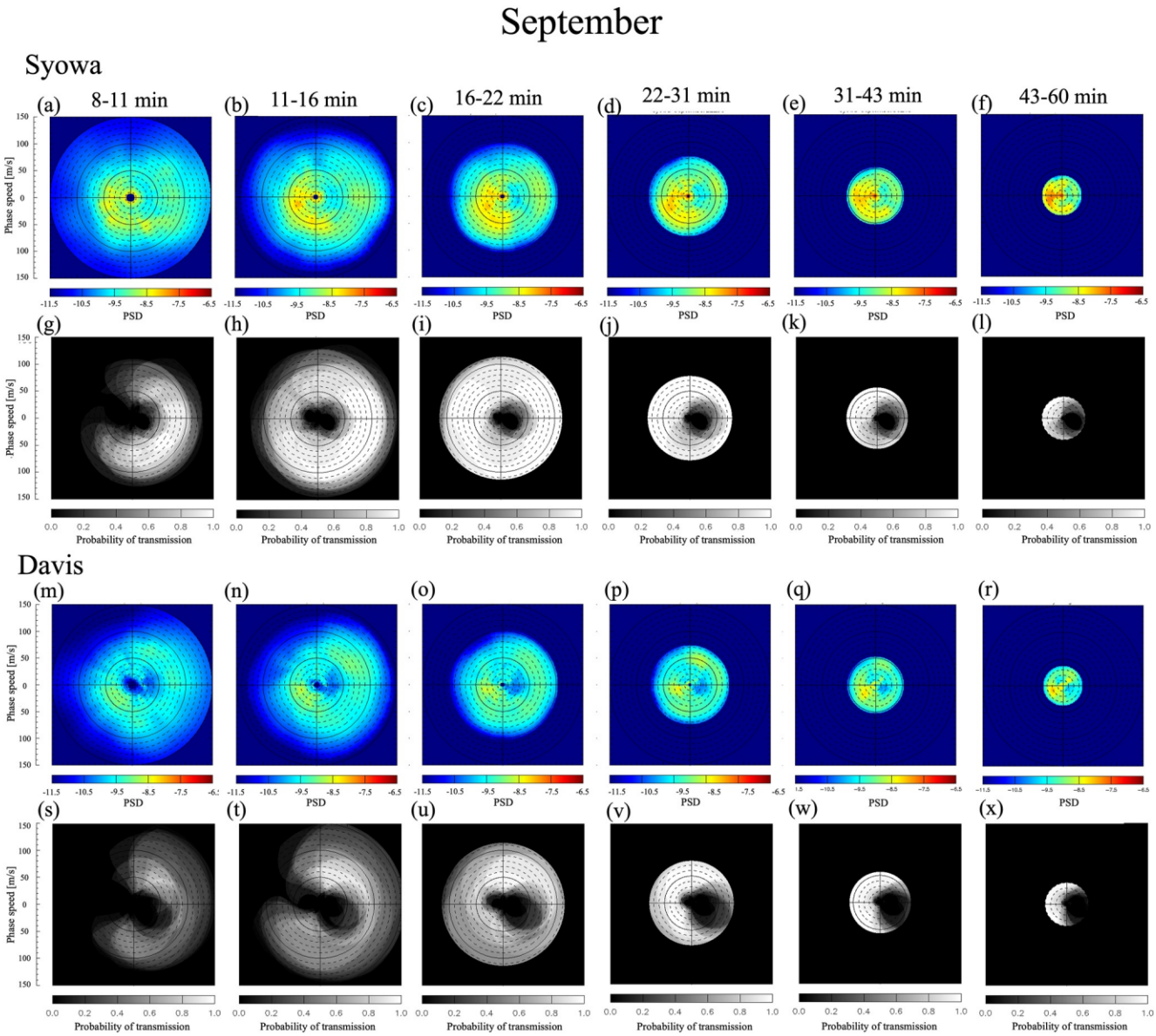

Figure 5. Same as Figure 4 but in September.

This chapter focuses on GWs at Davis on 29 August 2016, that originated from altitudes higher than ~45 km and investigates their sources.

5.1. Origin Altitudes of GWs on 29 August 2016

Intense GWs with east to southward (90 – 180° clockwise from the north) phase velocity higher than ~ 50 ms^{-1} were observed at Davis on 29 August 2016, but not observed at Syowa. Figure 6 shows the one-night mean spectra on August 29 at Syowa and Davis. The spectral powers at Syowa and Davis were concentrated in the southwest direction for waves with phase velocities between ~20 and 60 ms^{-1}. However, the spectral power of waves with southeastward phase velocities between 80 and 120 ms^{-1} were larger at Davis than at Syowa.

To explore where the GWs with ~100 ms^{-1} southeastward phase velocity came from, we applied a backward raytracing (Kogure et al., 2018, 2020). The initial horizontal wavelength (λ_H), ground-based period (τ), ground-based phase speed (C_h) are selected as values corresponding to the peaks of the power in ~30 ms^{-1} southwestward velocity spectra at Syowa and Davis, and ~100 ms^{-1} southeastward velocity spectra at Davis. Table 3

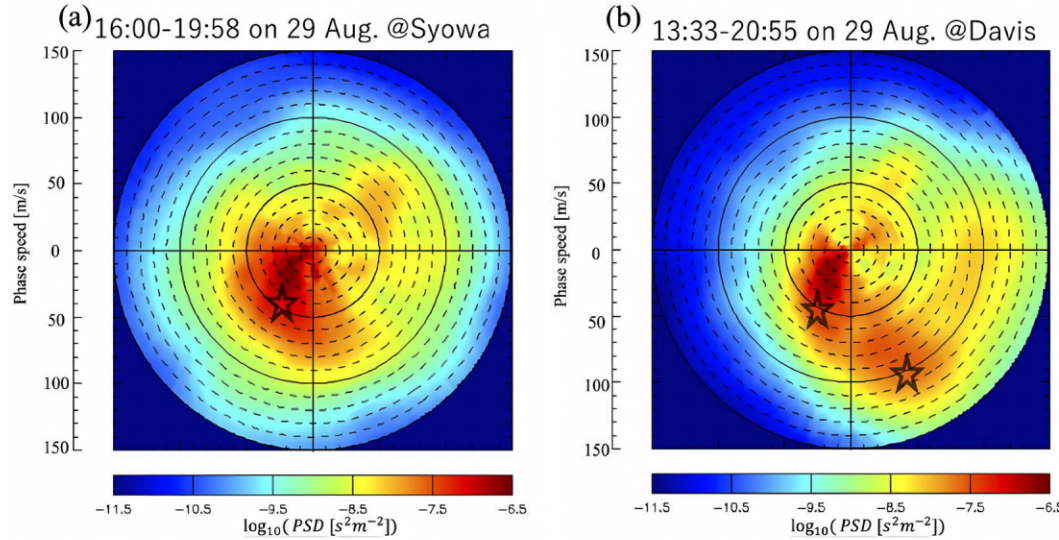

Figure 6. Power spectral density averaged on 29 August 2016, at Syowa (a) and Davis (b). The stars indicate initial phase velocities for the raytracing method.

shows the initial parameters. It should be noted that our raytracing model defines the ground-based frequency as positive (Dunkerton, 1984; Dunkerton & Butchart, 1984). The background wind and temperature below 70 km altitude were obtained from MERRA-2. Above the top of MERRA-2 (~74 km altitude), the background wind was measured by the MF radars, and the temperature was measured from Aura MLS. Between 70 km and the top of MERRA-2, a linear weighting function was used to average between MERRA-2 and the observations. It should be noted that horizontal wind shear effects on wavelength were neglected above the top of MERRA-2.

The backward raytracing results in Figure 7 show the three GW packets propagated from the Southern Ocean. While the S1 and D1 (southwestward phase velocities) could have propagated from 0.1 to 9.2 km altitudes, respectively, the D2 (southeastward phase velocity) back trace terminated at 44.5 km altitude because of a critical level. This result indicates that D2 must have been generated in the upper stratosphere or mesosphere. Rourke et al. (2017) observed GWs with eastward phase velocity over Davis. Their work showed that those waves originated from the upper stratosphere or mesosphere by using the raytracing method, although it used empirical model background fields and did not determine the wave sources.

5.2. The Possible GW Sources in the Upper Stratosphere and Mesosphere

The possible sources for the D2 GW (southeastward phase velocity) above ~45 km are (a) spontaneous adjustment (Becker et al., 2022; Plougonven & Zhang, 2014), and (b) secondary wave generation (Bühler et al., 1999; Chun & Kim, 2008; Dong et al., 2020; Franke & Robinson 1990; Fritts, 1984; Fritts et al., 2020; Heale et al., 2020, 2022; Kogure et al., 2020; Scinocca & Ford, 2000; Vadas & Becker, 2019; Vadas et al., 2003, 2018; Wilhelm et al., 2018; Zhou et al., 2002). To evaluate the possibility of the spontaneous adjustment, we calculated the residual of the nonlinear balance equation (ΔNBE), which indicates the degree of flow imbalance (Plougonven & Zhang, 2014), on its ray path using MERRA-2 fields. Figure 8 shows ΔNBE values averaged in 9–15 UT at 0.5 hPa (~50 km). The D2 GW passed over a high ΔNBE region with a value of $> 5 \times 10^{-9}$ s^{-1} (~67° E, ~66° S), suggesting the D2 GW may have been generated the imbalance flow in the upper stratosphere.

Table 3
Initial Raytracing Parameters for OH Layer Gravity-Waves

	No.	λ_H (km)	τ (min)	C_h (m/s)	Direction (degree)	Terminal height (km)
Syowa	S1	84	30	46	209	0.1
Davis	D1	28	9	52	207	9.2
	D2	88	14	103	156	44.5

Next, we evaluate the possibility of secondary generation. The Atmospheric Infrared Sounder (AIRS) aboard NASA's Aqua satellite captured two intense GW packets near the termination point (~42°E, ~58°S) at ~9:40 UT in the 15 μm high channel, which is most sensitive to GW temperature perturbations at ~38 km altitude in the polar region (Figure 9a). (Channel response data can be acquired from https://datapub.fz-juelich.de/slcs/airs/gravity_waves/:

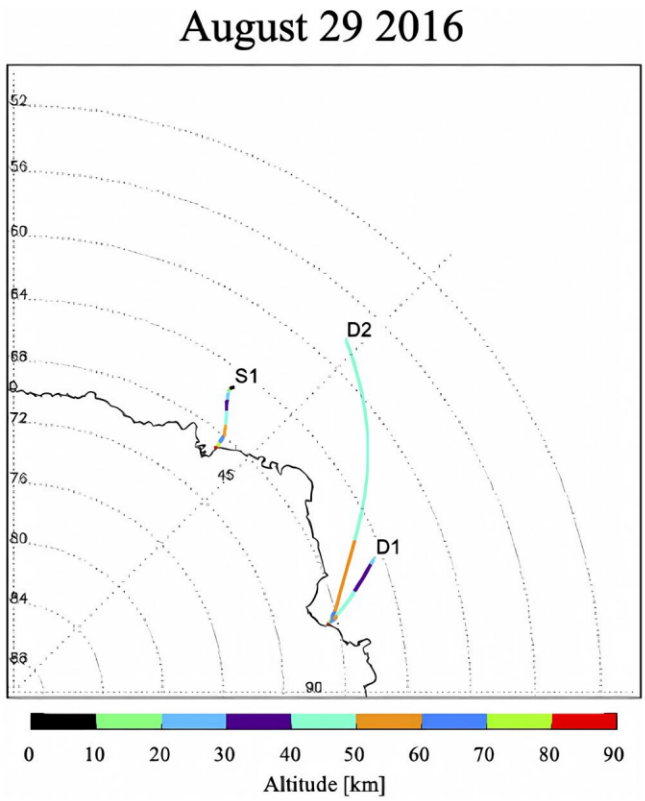

Figure 7. The backward raytracing results for the gravity-waves described in Table 3.

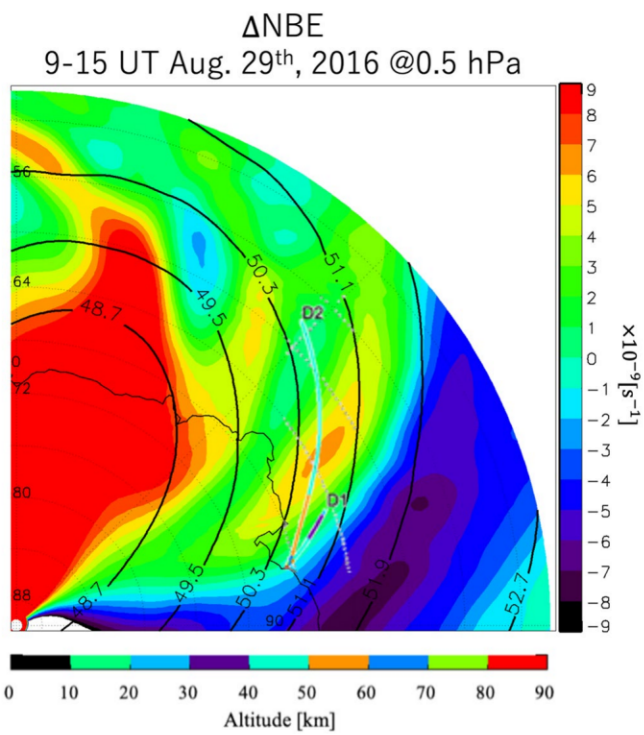

Figure 8. ΔNBE averaged in 9–15 UT at 0.5 hPa on 29th August 2016. Color lines denote the backward raytracing results for D1 and D2 waves.

Hoffman et al., 2013, 2017). The 15 μm low channel of AIRS, which is most sensitive to GW temperature perturbation at ~23 km altitude, also captured two intense GW packets in a similar area (Figure 9b).

These observed GWs appeared in the leeward of the geopotential height ridge at 200 hPa suggesting the waves were emitted from the tropospheric jet through spontaneous adjustment (Plougonven & Zhang, 2014). Indeed, we found that the ΔNBE value ($\sim 6 \times 10^{-9}\ s^{-1}$ at maximum) was enhanced around (~42°E, ~58°S), with a potential vorticity anomaly at 300 K (−9PVU) (not shown).

The AIRS data with 15 μm high channel were projected onto a km grid in Figure 10a. There are two GW packets apparent, with ~500 and ~200 km horizontal wavelengths. Packet sizes of the GWs with ~500 and 200 km are ~2,000 and ~500 km, respectively. The GW with ~2 K amplitude and ~200 km horizontal wavelength is situated near the termination of the D2 ray. If vertical wavelengths are much less than 24 km, AIRS significantly underestimates the true amplitude (Ern et al., 2017 (their Figure~S3); Hoffman et al., 2013, 2017).

Such intense GWs observed by AIRS could saturate and generate secondary GWs in the upper stratosphere and the mesosphere due to shear and/or convective instabilities (Bossert et al., 2015; Chun & Kim, 2008; Heale et al., 2020, 2022; Kogure et al., 2020; Song et al., 2003; Vadas & Becker, 2019; Vadas et al., 2003, 2018; Zhou et al., 2002.). To investigate the saturation of the GWs, we calculate the local Richardson number, Ri, along a forward ray path. This analysis is the same as Kogure et al. (2020) with the exception that our study assumes wave action conservation; previously it was assumed that the growth rate of wave amplitude was proportional to the inverse square root of density. To determine an initial horizontal wavenumber vector for the forward raytracing, the AIRS data in Figure 10a is subject to 2D Lomb-Scargle spectral analysis. Figure 10b shows the 2D Lomb-Scargle power spectrum where two local maxima in the spectrum can be seen. The local power maxima with 241 km horizontal wavelength and a direction of 146° (or 214°) clockwise from north correspond to the GW with ~200 km horizontal wavelength in Figures 9a and 10a. The 2D Lomb-Scargle analysis has 180° ambiguity, and for this reason we trialed both directions. A response rate of the AIRS high 15 μm kernel is estimated using the AIRS vertical kernel investigation (https://datapub.fz-juelich.de/slcs/airs/gravity_waves/data/kernel.pdf), and the amplitude of the raytraced GW was compensated accordingly. However, the response rate and peak of the AIRS kernel varies in location and season, which causes ambiguities of the amplitude and the altitude used to launch the ray. Due to these ambiguities, the response rate and the initial altitude are varied by 3% and 2 km, respectively. The AIRS instrument cannot observe the ground-based wave period, but an observable range of the ground-based period can be estimated from the shortest observable wavelengths of AIRS (~15 km) and the dispersion relation equation (Equation. 1c in Marks & Eckermann, 1995). The relation between the background wind and the horizontal ground-based phase velocity can be assumed to be one of the following cases: (1) the direction of the ground-based phase velocity is southeastward (146°), and its magnitude is less than the background wind (the ground-based period should be longer than ~3-hr), (2) the direction is the same as (1), but its magnitude is larger than the background wind (the ground-based period should be less than ~29-min), (3) the direction is northwestward (214°) (any ground-based period can be possible neglecting the upper limit of the verti-

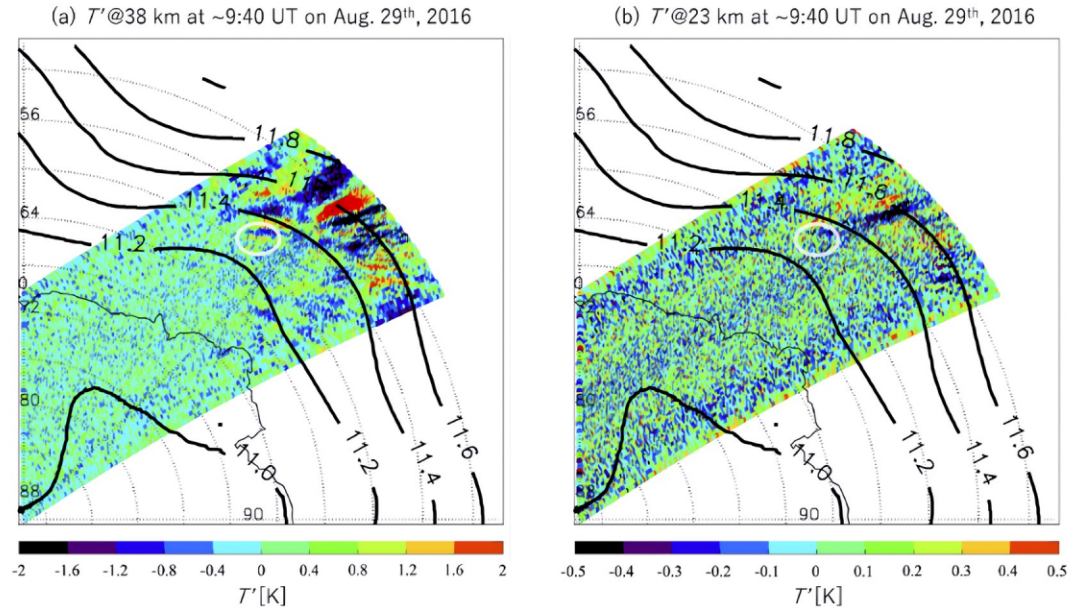

Figure 9. The Atmospheric Infrared Sounder (AIRS) temperature perturbations observed by AIRS at ~38 km (a) and ~23 km (b) at ~9:40 UT on 29 August 2016. The contour shows geopotential heights at 200 hPa. The white circle corresponds to the termination of D2 wave.

cal wavenumber). Here, the ground-based period was trialed at two values for each case selected according to saturation behavior; we do not find a saturation point of a GW below 50 km in case (1) with the ground-based period longer than 5 hr, case (2) with the period shorter than 24 min, and case (3) with the period shorter than 10 hr.

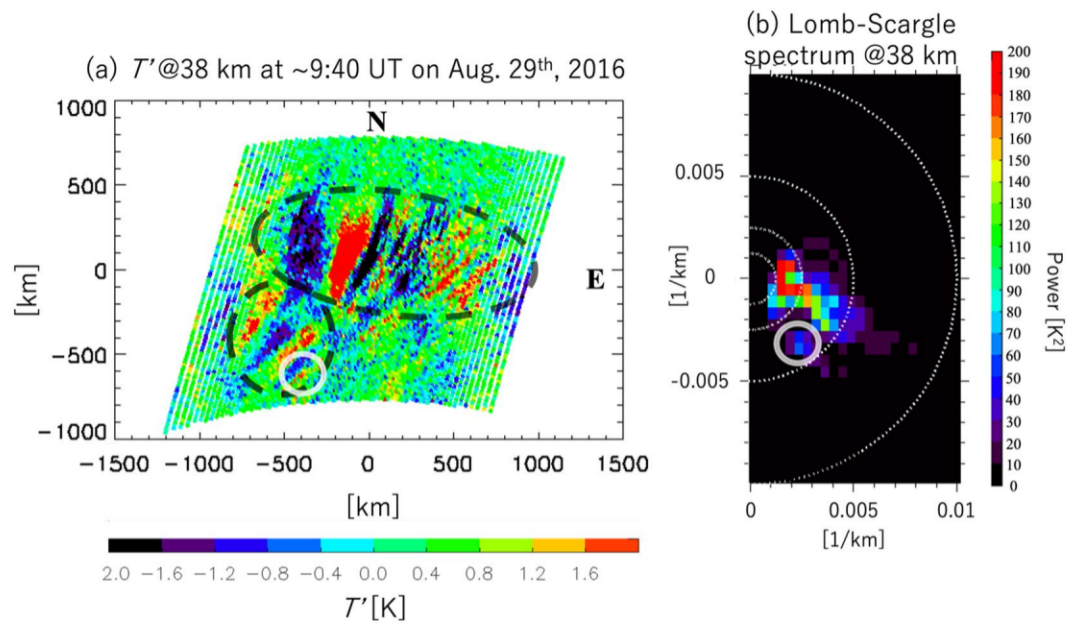

Figure 10. (a) The Atmospheric Infrared Sounder (AIRS) temperature perturbations in 25–62°E, 46–60°S projected onto a km grid at ~38 km. The black circles denote wave packets, and the white circle denotes the termination of the D2 wave. (b) The 2D Lomb-Scargle power spectrum of the AIRS temperature perturbations in 10–75°E, 46–60°S at ~38 km. The white circle denotes a spectrum corresponding to a wave packet which was present around the D2 wave terminal point. The white dashed lines denote isolines of horizontal wavelengths (100, 200, 400 k, and 800 km).

Table 4
Parameters for Gravity-Waves With a 241 km Horizontal Wavelength in the Atmospheric Infrared Sounder Data on 29 August 2016

Ground-based period (hour)	Initial altitude	Response rate of AIRS kernel (%)	Initial amplitude (K)	Bottom height Ri < 0.25 (km)	Initial vertical wavelength (km)
Case (1) the direction of the wave is southeast ward, and its phase speed is less than the background wind					
3	36	10 (7, 13)	20 (29, 15)	46 (39, 49)	16
3	38	10 (7, 13)	20 (29, 15)	48 (41, 59)	16
3	40	10 (7, 13)	20 (29, 15)	49 (46, 51)	16
5	36	14 (11, 17)	14 (18, 12)	50 (48, 51)	18
5	38	16 (13, 19)	13 (15, 11)	51 (51, 53)	19
5	40	16 (13, 19)	13 (15, 11)	53 (52, 56)	19
Ground-based period (min)	Initial altitude	Response rate of AIRS kernel (%)	Initial amplitude (K)	Bottom height Ri < 0.25 (km)	Initial vertical wavelength (km)
(2) the direction is the same as (1) but its phase speed is larger than the background wind					
24	36	8 (7, 10)	24 (27, 21)	No (No, No)	24
24	38	8 (7, 10)	24 (27, 21)	No (No, No)	24
24	40	8 (7, 10)	24 (27, 21)	No (No, No)	24
29	36	10 (7, 13)	20 (29, 15)	44 (38, 61)	16
29	38	10 (7, 13)	20 (29, 15)	45 (40, 62)	16
29	40	10 (7, 13)	20 (29, 15)	58 (42, 64)	16
Ground-based period (hour)	Initial altitude	Response rate of AIRS kernel (%)	Initial amplitude (K)	Bottom height Ri < 0.25 (km)	Initial vertical wavelength (km)
Case (3) the direction is northwest ward					
10	36	9 (8, 11)	22 (25, 19)	71 (72, 70)	24
10	38	8 (10, 7)	24 (21, 27)	72 (71, 73)	25
10	40	8 (10, 7)	24 (21, 27)	73 (72, 73)	25
Infinity	36	10 (8, 12)	20 (23, 17)	69 (71, 69)	22
Infinity	38	9 (8, 11)	22 (25, 19)	70 (69, 71)	23
Infinity	40	9 (8, 11)	22 (25, 19)	71 (72, 70)	23

Note. The initial amplitudes are 2 K (which is observed by AIRS) × the inverse of the response rate of the AIRS vertical kernel (https://datapub.fz-juelich.de/slcs/airs/gravity_waves/data/kernel.pdf). The values in parentheses are corresponding to the response rate −3% and +3%, respectively.

The altitudes at which Ri < 0.25 for the trial GWs, corresponding to the potential start of saturation, are given in Table 4. Figure 11 shows the forward raytracing result for the GW with 3-hr ground-based period from 38 km altitude. This GW began to be saturated at almost the same point (diamond mark) as the D2 termination (white circle) on the horizontal surface although the saturation altitude is ∼3 km higher than the D2 termination altitude. Agreement between the D2 termination height and the saturation height is not necessary because the D2 wave could have been launched above the backward ray tracing termination height (but not below). Although the GWs in cases (1) and (2) launched from similar horizontal positions but with the other parameters also propagated in the same direction (i.e., toward Davis), the propagation paths and saturation altitudes varied. The saturation altitudes of the GWs with the 3-hr and 29 min (case 1 and 2) ground-based periods were closer to altitudes of the D2 path than those for the other ground-based periods. On the other hand, the GWs in the case (3) do not meet the shear instability criterion. Therefore, those GWs in AIRS could be saturated assuming that they had the southeastward horizontal ground-based phase velocity with the ∼3-hr/∼29 min ground-based period. The eastward ground-based velocity is more reasonable than the westward velocity because the phase velocity of a GW emitted from a jet is expected to match the phase velocity of a baroclinic wave, that is, eastward (Plougonven & Snyder, 2007). Also, Murphy et al. (2014) occasionally observed GWs with eastward and 22 ms^{-1} phase

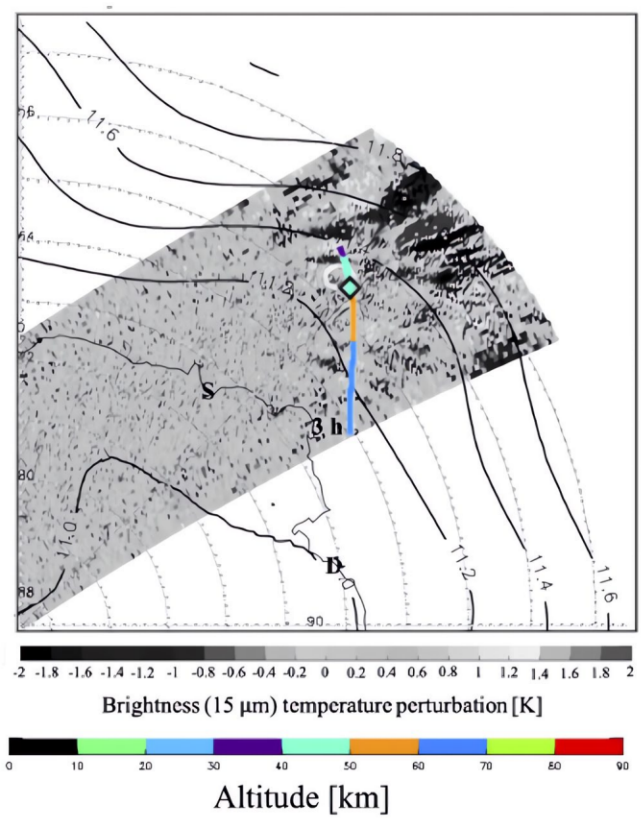

Figure 11. Raytracing result for the gravity-waves with southeast horizontal wavevector superimposed in Figure 9a. Its ground-based period, initial height, and initial temperature amplitude were assumed as 3 hr, 38 km, and 20 K, respectively. The diamond indicates a bottom altitude with Ri < 0.25.

speed (=241 km/3 hr) in the lower stratosphere over Davis that are consistent with the wave shown in Figure 11. Making the assumption that the southeastward propagating GW in the AIRS data had ~3-hr/29-min ground-based period, it can be asserted that the wave saturated at ~45–50 km; therefore, the GWs with ~100 ms^{-1} southeastward phase velocity at Davis (D2 in Figure 7) could be secondary GWs caused by breaking of the tropospheric jet GWs.

Heale et al. (2022) classified secondary GWs into three scale types of secondary GWs: GWs with horizontal wavelengths smaller than, similar to, and longer than a horizontal wavelength of a primary GW. Because the horizontal wavelength of D2 wave (~88 km) is ~3 times smaller than that of the jet GWs (~241 km), the D2 wave could be corresponding to the smaller-scale secondary GWs in Heale et al. (2022). This type of GW is generated by localized forcing, whose scales are associated with instability and vortex scales, produced by a primary GW breaking (Chun & Kim, 2008; Franke & Robinson 1990; Heale et al., 2020, 2022; Snively & Pasko, 2003; Song et al., 2003; Vadas & Becker, 2019; Zhou et al., 2002.). Therefore, the jet GWs possibly caused instabilities with scales similar to the D2 wave's horizontal wavelength (~88 km).

In summary, our raytracing simulation shows that the GWs with ~100 ms^{-1} southeastward phase velocity, observed by the OH imager at Davis, was generated above ~45 km over the Southern Ocean. Those GWs were probably caused by the spontaneous adjustment at ~50 km or/and breaking of GWs, emitted from the tropospheric jet, at ~45–50 km.

6. Conclusion

We compared the GW total powers and phase velocity spectra in the OH layer at two Antarctic stations, Davis and Syowa, from March to October 2016. The total powers showed maxima in winter and have similar seasonal variation at both stations. Also, both winter mean spectra showed the same characteristics, that is, large PSDs in $\leq\sim 50\ ms^{-1}$ eastward phase velocity and $\geq 80\ ms^{-1}$ westward phase velocity domains. Those characteristics could be caused by the polar night jet, implying that the jet strongly controls the Antarctic GW propagation over the Antarctic as is well known.

While the winter mean powers at both stations were not significantly different, the total power at Davis was three times lower than that at Syowa. The lower power at Davis in September was attributed to weaker GWs with omnidirectional phase velocity. To evaluate background meteorological field impacts on the GWs at both stations, we compared the spectra and probability diagrams of wave transmission and found that the transmission probability in Davis was lower than that at Syowa, suggesting that the filtering effects can explain the lower power at Davis in September.

We also investigated potential sources in the middle atmosphere. Our raytracing simulation showed GWs with 100 ms^{-1} southeastward phase velocity, observed by the OH imager at Davis on 29th August 2016, were generated above ~45 km over the Southern Ocean (~43°E, ~ 58°S). Those GWs with southeastward phase velocity were probably caused by the spontaneous adjustment at ~50 km or/and breaking of GWs emitted from the tropospheric jet at 45–50 km. The spontaneous adjustment and breaking of primary waves might occasionally cause GWs in the middle atmosphere (indeed some studies reported GWs originated from the Antarctic middle atmosphere in OH imager data) although more observational evidence is needed.

Data Availability Statement

MERRA-2 data were obtained at http://disc.sci.gsfc.nasa.gov [Dataset] (GMAO, 2015a, 2015b). MLS_Aura data were obtained at https://mls.jpl.nasa.gov/index-eos-mls.php [Dataset] (Waters et al., 2006). The AIRS/Aqua gravity wave data sets (Hoffmann et al., 2017) are provided by Forschungszentrum Jülich (https://datapub.fz-jue-

lich.de/slcs/airs/gravity_waves/data [Dataset]). The daily average phase velocity spectra data at both stations can be obtained at https://doi.org/10.5281/zenodo.7325405 [Dataset]. The MF radar data averaged in winter and September can be obtained at https://doi.org/10.5281/zenodo.7325416 [Dataset]. The M-transform program can be obtained at http://polaris.nipr.ac.jp/~airglow/M-transform/ [Software] (Perwitasari et al., 2018).

Acknowledgments
This work is supported by the JSPS grant JRPs-LEAD with DFG program (JPJSJRP 20181602), JSPS KAKENHI Grant JP15H02137, JP19K23465 and JP22J00331, JSPS Overseas Challenge Program for Young Researchers (No. 201780038), ROIS-DS-JOINT (046RP2022), 2022 Research Start Program 202204, and the Scientific Committee on Antarctic Research (SCAR) fellowship award 2019. Support for the operation of the Davis MF radar and its analysis was provided through AAS project number 4025, 4056, and 4445. The USU all-sky OH imager operated at Davis Station and its data analysis are supported by NSF 1143587 and NSF 1443730.

References

Alexander, M. J., Geller, M., McLandress, C., Polavarapu, S., Preusse, P., Sassi, F., et al. (2010). Recent developments in gravity-wave effects in climate models and the global distribution of gravity-wave momentum flux from observations and models. *Quarterly Journal of the Royal Meteorological Society*, *136*(650), 1103–1124. https://doi.org/10.1002/qj.637

Baker, D. J., & Stair, A. T., Jr. (1988). Rocket measurements of the altitude distributions of the hydroxyl airglow. *Physica Scripta*, *37*(4), 611–622. https://doi.org/10.1088/0031-8949/37/4/021

Becker, E., Vadas, S. L., Bossert, K., Harvey, V. L., Zülicke, C., & Hoffmann, L. (2022). A High-resolution whole-atmosphere model with resolved gravity waves and specified large-scale dynamics in the troposphere and stratosphere. *Journal of Geophysical Research: Atmospheres*, *127*(2), e2021JD035018. https://doi.org/10.1029/2021JD035018

Bossert, K., Fritts, D. C., Pautet, P.-D., Williams, B. P., Taylor, M. J., Kaifler, B., et al. (2015). Momentum flux estimates accompanying multiscale gravity waves over Mount Cook, New Zealand, on 13 July 2014 during the DEEPWAVE campaign. *Journal of Geophysical Research: Atmospheres*, *120*(18), 9323–9337. https://doi.org/10.1002/2015JD023197

Bossert, K., Kruse, C. G., Heale, C. J., Fritts, D. C., Williams, B. P., Snively, J. B., et al. (2017). Secondary gravity wave generation over New Zealand during the DEEPWAVE campaign. *Journal of Geophysical Research: Atmospheres*, *122*(15), 7834–7850. https://doi.org/10.1002/2016JD026079

Bühler, O., McIntyre, M. E., & Scinocca, J. F. (1999). On shear-generated gravity waves that reach the mesosphere. Part I: Wave generation. *Journal of the Atmospheric Sciences*, *56*(21), 3749–3763. https://doi.org/10.1175/1520-0469(1999)056<3749:osggwt>2.0.co;2

Chun, H.-Y., & Kim, Y.-H. (2008). Secondary waves generated by breaking of convective gravity waves in the mesosphere and their influence in the wave momentum flux. *Journal of Geophysical Research*, *113*(D23), D23107. https://doi.org/10.1029/2008JD009792

Dong, W., Fritts, D. C., Lund, T. S., Wieland, S. A., & Zhang, S. (2020). Self-acceleration and instability of gravity wave packets: 2. Two-dimensional packet propagation, instability dynamics, and transient flow responses. *Journal of Geophysical Research: Atmospheres*, *125*(3), e2019JD030691. https://doi.org/10.1029/2019jd030691

Dunkerton, T. J. (1984). Inertia–gravity waves in the stratosphere. *Journal of the Atmospheric Sciences*, *41*(23), 3396–3404. https://doi.org/10.1175/1520-0469(1984)041<3396:iwits>2.0.co;2

Dunkerton, T. J., & Butchart, N. (1984). Propagation and selective transmission of internal gravity waves in a sudden warming. *Journal of the Atmospheric Sciences*, *41*(8), 1443–1460. https://doi.org/10.1175/1520-0469(1984)041<1443:pastoi>2.0.co;2

Ern, M., Hoffmann, L., & Preusse, P. (2017). Directional gravity wave momentum fluxes in the stratosphere derived from high-resolution AIRS temperature data. *Geophysical Research Letters*, *44*(1), 475–485. https://doi.org/10.1002/2016GL072007

Franke, P. M., & Robinson, W. A. (1990). Nonlinear behavior in the propagation of atmospheric gravity waves. *Journal of the Atmospheric Sciences*, *56*(17), 3010–3027. https://doi.org/10.1175/1520-0469(1999)056<3010:NBITPO>2.0.CO;2>

Fritts, D. C. (1984). Gravity wave saturation in the middle atmosphere: A review of theory and observations. *Review of Geophysics*, *22*(3), 275–308. https://doi.org/10.1029/RG022i003p00275

Fritts, D. C., & Alexander, M. J. (2003). Gravity wave dynamics and effects in the middle atmosphere. *Reviews of Geophysics*, *41*, 1003. https://doi.org/10.1029/2001RG000106

Fritts, D. C., Dong, W., Lund, T. S., Wieland, S., & Laughman, B. (2020). Self-acceleration and instability of gravity wave packets: 3. Three-dimensional packet propagation, secondary gravity waves, momentum transport, and transient mean forcing in tidal winds. *Journal of Geophysical Research: Atmospheres*, *125*, e2019JD030692. https://doi.org/10.1029/2019jd030692

Fritts, D. C., & Vincent, R. A. (1987). Mesospheric momentum flux studies at Adelaide, Australia: Observations and a gravity wave–tidal interaction model. *Journal of the Atmospheric Sciences*, *44*(3), 605–619. https://doi.org/10.1175/1520-0469(1987)044<0605:MMFSAA>2.0.CO;2>

Gelaro, R., McCarty, W., Suárez, M. J., Todling, R., Molod, A., Takacs, L., et al. (2017). The modern-era retrospective analysis for research and applications, version 2 (MERRA-2). *Journal of Climate*, *30*(14), 5419–5454. https://doi.org/10.1175/JCLI-D-16-0758.1

Global Modeling, & Assimilation Office (GMAO). (2015a). *MERRA-2 inst3_3d_asm_Np: 3d,3-hourly, instantaneous, pressure-level, assimilation, assimilated meteorological fields V5.12.4*. Goddard Earth Sciences Data and Information Services Center (GES DISC). https://doi.org/10.5067/QBZ6MG944HW0

Global Modeling and Assimilation Office (GMAO). (2015b). *MERRA-2 inst3_3d_asm_Nv: 3d,3-hourly, instantaneous, model-level, assimilation, assimilated meteorological fields V5.12.4*. Goddard Earth Sciences Data and Information Services Center (GES DISC). https://doi.org/10.5067/WWQSXQ8IVFW8

Grygalashvyly, M., Sonnemann, G. R., Lübken, F.-J., Hartogh, P., & Berger, U. (2014). Hydroxyl layer: Mean state and trends at midlatitudes. *Journal of Geophysical Research: Atmospheres*, *119*(21), 12391–12419. https://doi.org/10.1002/2014JD022094

Heale, C. J., Bossert, K., Snively, J. B., Fritts, D. C., Pautet, P.-D., & Taylor, M. J. (2017). Numerical modeling of a multiscale gravity wave event and its airglow signatures over Mount Cook, New Zealand, during the DEEPWAVE campaign. *Journal of Geophysical Research: Atmospheres*, *122*(2), 846–860. https://doi.org/10.1002/2016JD025700

Heale, C. J., Bossert, K., & Vadas, S. L. (2022). 3D numerical simulation of secondary wave generation from mountain wave breaking over Europe. *Journal of Geophysical Research: Atmospheres*, *127*(5), e2021JD035413. https://doi.org/10.1029/2021JD035413

Heale, C. J., Bossert, K., Vadas, S. L., Hoffmann, L., Dörnbrack, A., Stober, G., et al. (2020). Secondary gravity waves generated by breaking mountain waves over Europe. *Journal of Geophysical Research: Atmospheres*, *125*(5), e2019JD031662. https://doi.org/10.1029/2019JD031662

Hoffmann, L., Spang, R., Orr, A., Alexander, M. J., Holt, L. A., & Stein, O. (2017). A decadal satellite record of gravity wave activity in the lower stratosphere to study polar stratospheric cloud formation. *Atmospheric Chemistry and Physics*, *17*(4), 2901–2920. https://doi.org/10.5194/acp-17-2901-2017

Hoffmann, L., Xue, X., & Alexander, M. J. (2013). A global view of stratospheric gravity wave hotspots located with Atmospheric Infrared Sounder observations. *Journal of Geophysical Research: Atmospheres*, *118*(2), 416–434. https://doi.org/10.1029/2012JD018658

Kam, H., Song, I.-S., Kim, J.-H., Kim, Y. H., Song, B.-G., Nakamura, T., et al. (2021). Mesospheric short-period gravity waves in the Antarctic Peninsula observed in all-sky airglow images and their possible source locations. *Journal of Geophysical Research: Atmospheres*, *126*(24), e2021JD035842. https://doi.org/10.1029/2021JD035842

Kogure, M., Nakamura, T., Ejiri, M. K., Nishiyama, T., Tomikawa, Y., & Tsutsumi, M. (2018). Effects of horizontal wind structure on a gravity wave event in the middle atmosphere over Syowa (69°S, 40°E), the Antarctic. *Geophysical Research Letters*, *45*(10), 5151–5157. https://doi.org/10.1029/2018GL078264

Kogure, M., Yue, J., Nakamura, T., Hoffmann, L., Vadas, S. L., Tomikawa, Y., et al. (2020). First direct observational evidence for secondary gravity waves generated by mountain waves over the Andes. *Geophysical Research Letters*, *47*(17), e2020GL088845. https://doi.org/10.1029/2020GL088845

Marks, C. J., & Eckermann, S. D. (1995). A three-dimensional nonhydrostatic ray-tracing model for gravity waves: Formulation and preliminary results for the middle atmosphere. *Journal of the Atmospheric Sciences*, *52*(11), 1959–1984. https://doi.org/10.1175/1520-0469(1995)052<1959:ATDNRT>2.0.CO;2>

Matsuda, T. S., Nakamura, T., Ejiri, M. K., Tsutsumi, M., & Shiokawa, K. (2014). New statistical analysis of the horizontal phase velocity distribution of gravity waves observed by airglow imaging. *Journal of Geophysical Research: Atmospheres*, *119*(16), 9707–9718. https://doi.org/10.1002/2014JD021543

Matsuda, T. S., Nakamura, T., Ejiri, M. K., Tsutsumi, M., Tomikawa, Y., Taylor, M. J., et al. (2017). Characteristics of mesospheric gravity waves over Antarctica observed by Antarctic Gravity Wave Instrument Network imagers using 3-D spectral analyses. *Journal of Geophysical Research: Atmospheres*, *122*(17), 8969–8981. https://doi.org/10.1002/2016JD026217

Murphy, D. J., Alexander, S. P., Klekociuk, A. R., Love, P. T., & Vincent, R. A. (2014). Radiosonde observations of gravity waves in the lower stratosphere over Davis, Antarctica. *Journal of Geophysical Research: Atmospheres*, *119*(21), 11973–11996. https://doi.org/10.1002/2014JD022448

Nishiyama, T., Taguchi, M., Suzuki, H., Dalin, P., Ogawa, Y., Brändström, T., & Sakanoi, T. (2021). Temporal evolutions of N2+Meinel (1,2) band near 1.5.μm associated with aurora breakup and their effects on mesopause temperature estimations from OH Meinel (3,1) band. *Earth Planets and Space*, *73*(1), 30. https://doi.org/10.1186/s40623-021-01360-0

Perwitasari, T. N., Kogure, M., Tomikawa, Y., Ejiri, M. K., Shiokawa, K., & Shiokawa, K. (2018). Comparison of gravity wave propagation directions observed by mesospheric airglow imaging at three different latitudes using the M-transform. *Annales Geophysicae*, *36*(6), 1597–1605. https://doi.org/10.5194/angeo-36-1597-2018

Plougonven, R., & Snyder, C. (2007). Inertia–gravity waves spontaneously generated by jets and fronts. Part I: Different baroclinic life cycles. *Journal of the Atmospheric Sciences*, *64*(7), 2502–2520. https://doi.org/10.1175/JAS3953.1

Plougonven, R., & Zhang, F. (2014). Internal gravity waves from atmospheric jets and fronts. *Reviews of Geophysics*, *52*(1), 33–76. https://doi.org/10.1002/2012RG000419

Rourke, S., Mulligan, F. J., French, W. J. R., & Murphy, D. J. (2017). A climatological study of short-period gravity waves and ripples at Davis Station, Antarctica (68°S, 78°E), during the (austral winter February–October) period 1999–2013. *Journal of Geophysical Research: Atmospheres*, *122*(21), 11388–11404. https://doi.org/10.1002/2017JD026998

Scinocca, J. F., & Ford, R. (2000). The nonlinear forcing of large-scale internal gravity waves by stratified shear instability. *Journal of the Atmospheric Sciences*, *57*(5), 653–672. https://doi.org/10.1175/1520-0469(2000)057<0653:tnfols>2.0.co;2

Snively, J. B., & Pasko, V. P. (2003). Breaking of thunderstorm-generated gravity waves as a source of short-period ducted waves at mesopause altitudes. *Geophysical Research Letters*, *30*(24), 2254. https://doi.org/10.1029/2003GL018436

Song, I. S., Chun, H.-Y., & Lane, T. P. (2003). Generation mechanisms of convectively forced internal gravity waves and their propagation to the stratosphere. *Journal of the Atmospheric Sciences*, *60*(16), 1960–1980. https://doi.org/10.1175/1520-0469(2003)060<1960:GMOCFI>2.0.CO;2>

Tomikawa, Y. (2015). Gravity wave transmission diagram. *Annales Geophysicae*, *33*(12), 1479–1484. https://doi.org/10.5194/angeo-33-1479-2015

Tsutsumi, M., Aso, T., & Ejiri, M. (2001). Initial results of Syowa MF radar observations in Antarctica. *Advances in Polar Upper Atmosphere Research*, *15*, 103–116. https://doi.org/10.15094/00006333

Vadas, S. L., & Becker, E. (2019). Numerical modeling of the generation of tertiary gravity waves in the mesosphere and thermosphere during strong mountain wave events over the Southern Andes. *Journal of Geophysical Research: Space Physics*, *124*(9), 7687–7718. https://doi.org/10.1029/2019ja026694

Vadas, S. L., Fritts, D. C., & Alexander, M. J. (2003). Mechanism for the generation of secondary waves in wave breaking regions. *Journal of the Atmospheric Sciences*, *60*(1), 194–214. https://doi.org/10.1175/1520-0469(2003)060<0194:MFTGOS>2.0.CO;2

Vadas, S. L., Zhao, J., Chu, X., & Becker, E. (2018). The excitation of secondary gravity waves from local body forces: Theory and observation. *Journal of Geophysical Research: Atmospheres*, *123*(17), 9296–9325. https://doi.org/10.1029/2017JD027970

Waters, J. W., Froidevaux, L., Harwood, R. S., Jarnot, R. F., Pickett, H. M., Read, W. G., et al. (2006). The Earth observing system microwave limb sounder (EOS MLS) on the aura Satellite. *IEEE Transactions on Geoscience and Remote Sensing*, *44*(5), 1075–1092. https://doi.org/10.1109/TGRS.2006.873771

Wilhelm, J., Akylas, T. R., Bölöni, G., Wei, J., Ribstein, B., Klein, R., & Achatz, U. (2018). Interactions between mesoscale and submesoscale gravity waves and their efficient representation in mesoscale-resolving models. *Journal of the Atmospheric Sciences*, *75*(7), 2257–2280. https://doi.org/10.1175/JAS-D-17-0289.1

Zhou, X.-L., Holton, J. R., & Mullendore, G. L. (2002). Forcing of secondary waves by breaking of gravity waves in the mesosphere. *Journal of Geophysical Research*, *107*(D7). 4058. https://doi.org/10.1029/2001JD001204